frontiers | Frontiers in Materials

TYPE Original Research
PUBLISHED 28 September 2022
DOI 10.3389/fmats.2022.952631

OPEN ACCESS

EDITED BY
Bing Bai,
Beijing Jiaotong University, China

REVIEWED BY
Chunhui Ma,
Xi'an University of Technology, China
Jianyong Han,
Shandong Jianzhu University, China
Chen Peipei,
Beijing University of Civil Engineering and Architecture, China

*CORRESPONDENCE
Gao Lv,
lvgao116@qq.com
Naifei Liu,
liunaifei1985@126.com

SPECIALTY SECTION
This article was submitted to Structural Materials,
a section of the journal
Frontiers in Materials

RECEIVED 25 May 2022
ACCEPTED 10 August 2022
PUBLISHED 28 September 2022

CITATION
Lv G, Liu N, Bao L, Yang B and Zhang Y (2022), Detection of cracks in cemented loess of ancient buildings using remote sensing.
Front. Mater. 9:952631.
doi: 10.3389/fmats.2022.952631

Detection of cracks in cemented loess of ancient buildings using remote sensing

Gao Lv[1,2,3]*, Naifei Liu[2,4]*, Liangliang Bao[5], Bei Yang[6] and Yafei Zhang[1,3]

[1]School of Civil Engineering, Xi'an Shiyou University, Xi'an, China, [2]Shaanxi Key Laboratory of Geotechnical and Underground Space Engineering, XAUAT, Xi'an, China, [3]Xi'an Key Laboratory of Wellbore Integrity Evaluation, Xi'an Shiyou University, Xi'an, China, [4]School of Civil Engineering, Xi'an University of Architecture and Technology, Xi'an, China, [5]School of Civil Engineering, Yulin University, Yulin, China, [6]Architectural Design and Research Institute, Xi'an University of Architecture and Technology, Xi'an, China

The bases of ancient Chinese buildings are prone to deformation, cracks, and other hidden problems due to their age and other reasons. Rainfall and water seepage produce great harm to the cracks of soil plinths. Based on a ground-penetrating radar method, detecting cracks and water erosion defects is important for protecting ancient buildings. This study examines the reflection characteristics of ground-penetrating radar (GPR) waves at different lithological interfaces. Physical experiments and their numerical and physical laws were used to study the reflection characteristics of GPR incidents from brick to air, unsaturated soil, water, and metal interfaces. The model was applied to detect defects of the Xi'an Bell Tower and the main research results are as follows. The echo amplitude of GPR was positively correlated with the relative permittivity of the bedding layer, and its basic law conforms to the positive logarithmic curve. The hyperbolic opening of water erosion imaging of the base-compacted soil is larger, the attenuation effect increases and the signal reflection is obvious. These results provide the theoretical basis and technical support for the actual detection of water erosion deterioration of loess in similar projects, and this provides theoretical and technical references for rapid identification and management of defects in ancient buildings.

KEYWORDS

ground-penetrating radar, relative permittivity, GPR characterization, finite difference time domain method, ancient buildings

Introduction

Ancient Chinese architecture has a long history and is a remarkable architectural style (Xue, 2010). Globally, it has a very high artistic and cultural value. However, the common structure of ancient Chinese architecture consists of wooden buildings and rammed Earth foundations. In particular, the masonry and rammed Earth-based foundations have been subjected to long-term erosion by the natural environment and the influence of human factors (Wang et al., 2017). Therefore, this has led to a series of irreversible damages such

as cracks, breakage, cavitation, collapse, deformation (Liu et al., 2020a; Bai et al., 2021a), and concealed areas. There is an urgent need to implement early detection, early maintenance, early repair, and other measures for the protection of the appearance of ancient buildings and internal hidden problems (Liu et al., 2020b; Bai et al., 2021b).

The evaluation of the masonry footings of ancient buildings is more intuitive. However, identifying and excluding hidden defects of masonry table foundations are more difficult (Wang et al., 2020; Kang et al., 2021). For conservation, it is obvious that measures, such as drilling, cannot be blindly conducted on ancient Chinese buildings. Instead, it is more advantageous and wiser to use non-destructive geophysical methods. The current non-destructive methods for detecting ancient buildings are mainly Pilodyn, Resist graph, Impulse Tomography, GPR, and Hotpoint-line-surface methods (Lv et al., 2018a; Lv et al., 2018b). However, for the detection of water seepage and the location of damage of ancient buildings, GPR has advantages of portability, precision, and low cost (Adachi et al., 2020; Dao et al., 2020; Lieblappen et al., 2020; Khan et al., 2021). GPR can detect the internal structure of ancient buildings, identify possible cracks and cavities in the walls, and determine water seepage areas of ancient buildings (Cappuccio et al., 2020; Ziegler et al., 2020).

Recent research that has advanced GPR for the detection of ancient buildings is described below. Mallorca Cathedral (Elyamani et al., 2017; Elyamani et al., 2018; Elyamani et al., 2019) described the analysis of some structural elements' inner geometries and physical properties by GPR. Different problems, such as the characterization of the masonry, the detection of cracks, and the imaging of metallic reinforcement bars, were examined on three different constructive elements typical of historic buildings (Corradi et al., 2018; Stepinac et al., 2020). An experiment was conducted on samples of sawn timber of different species to study their dielectric responses according to the grain directions using a GPR with a 1.6 GHz antenna to assess the physical properties of wood structures (Fediuk et al., 2020; Wu et al., 2020). Respective signal and image analyses of GPR have enhanced their usefulness in the field of built cultural heritage protection (Solla et al., 2020; Adamopoulos and Rinaudo, 2021; Lombardi et al., 2021). The structure, construction techniques, materials, history, and pathologies in a classified Modern Age building were provided as *a priori* knowledge by GPR (Cardinali et al., 2021; Mishra, 2021). Moisture measurements of porous masonry elements were tested to assess their applicability by a stepped frequency GPR (Agliata et al., 2018; Lai et al., 2018). GPR is a building structure defect detection technology that has accurate and flexible characteristics. The above study uses the visual detection images of GPR as the basis for analysis and evaluation. There are also different frequency detection effect comparisons. However, we want to get more quantitative structural defect characteristics and not just qualitative expressions.

Presently, there are relatively few relevant analyses and studies of GPR imaging characteristics of the basic structure of brick and fill soil such as that at the Xi'an Bell Tower. In particular, there are relatively few studies on the imaging characteristics of problems such as hidden defects in the masonry of ancient buildings. In this study, physical experiments and numerical simulations of the interface between masonry and rammed Earth are used to establish the geoelectric model of the surface and bedding layers under different combinations of relative permittivity. We established an empirical model for the rapid calculation of volumetric moisture content at defect locations. This provides a basis for inference and interpretation during the actual measurement. This study helps to clarify the location and extent of the base breakage and more directly assesses the safety state of the brick and soil of ancient buildings. Additionally, it provides theoretical and technical references for rapid identification and management of defects in ancient buildings.

General description

The Xi'an Bell Tower, which is located in the center of Xi'an, China, is shown in Figure 1A. It was built in 1384 AD, and it is the largest and best-preserved bell tower among the existing bell towers in China (Lv et al., 2018b). In terms of architectural scale, historical value, and artistic value, it is the first of its kind in China. The total height of the Xi'an Bell Tower is 36 m and it covers an area of 1,377 m^2. The overall structure of the Xi'an Bell Tower is divided into three parts, the foundation, the square base, and the wooden building seen in Figure 1B. The foundation is the original pile of loess and residual ancient soil layer. The base is 35.5 m square and 8.6 m in height. The interior is a manually layered and compacted plain fill. The exterior is built with green bricks. The wooden building body is a three-story wooden structure with a height of 27.4 m (Qiu et al., 2020; Xie et al., 2020; Zhu et al., 2020; Hou et al., 2021).

For more than 600 years, there has been a combination of natural environmental erosion (such as wind and rain erosion, humidity and temperature changes), material aging, long-term effects of loading, and fatigue effects. The physical and mechanical properties of the table foundation have been degraded. Inevitably, the accumulation of damage and decay of resistance of the table foundation system (Ma and Wang, 2018; Lu et al., 2021) has occurred. The physical and mechanical properties of the foundation have been degraded. Meanwhile, the Xi'an Bell Tower is located in the traffic hub of Xi'an city. The continuous micro-amplitude vibration caused by long-term surface and underground construction (e.g., underground shopping malls, underground pedestrian passages, and subways) has caused fatigue of the ancient wooden structure and deformation and cracking of the

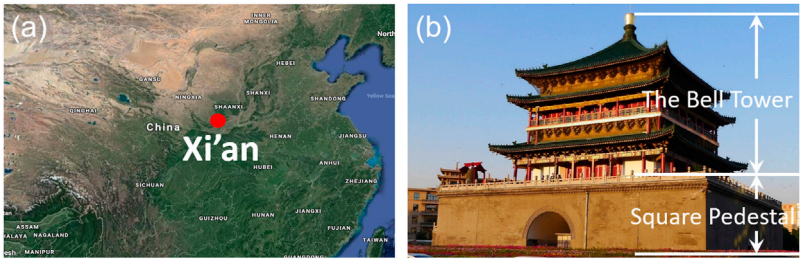

FIGURE 1
Location and the basic structure of the Xi'an Bell Tower.

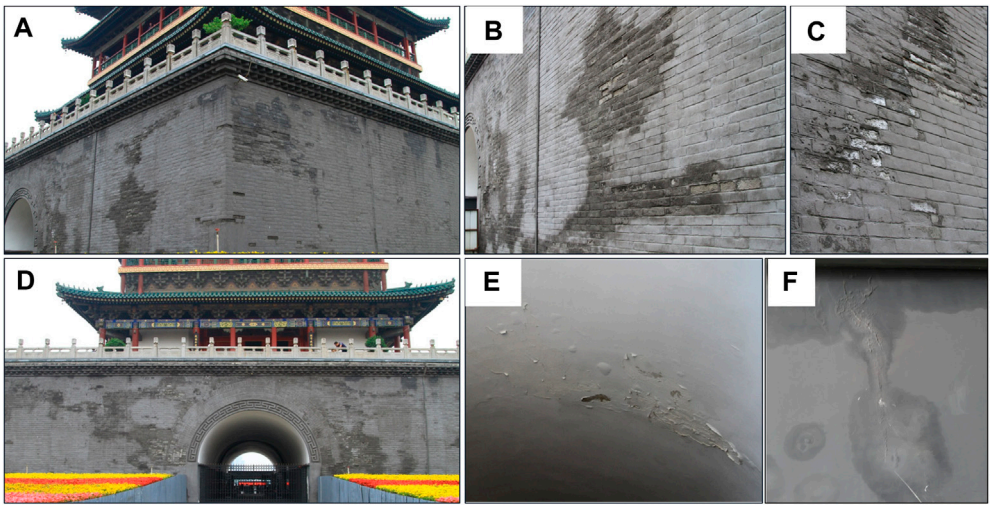

FIGURE 2
Water seepage on the exterior wall of the Xi'an Bell Tower pedestal **(A)** the southwest corner; **(B)** the west pedestal; **(C)** calcium precipitates; **(D)** the south pedestal; **(E)** the west archway; and **(F)** the east archway.

foundation (Luo et al., 2021). The infiltration of rainfall has caused water erosion and deterioration of the city bricks, plasterwork, steps, and rammed Earth layers (Bai et al., 2017; Bai et al., 2019; Bai et al., 2020; Bai et al., 2022). This seriously affects the long-term safety and stability of the Xi'an Bell Tower.

Figures 2A–D show the current condition of water seepage and masonry erosion on the side of the square base, and Figures 2E and F show the condition of water seepage and erosion in the cracks on the top of the archway. From the figures, it can be inferred that cracks exist in the plasterwork, which allows precipitation to seep into the interior of the foundation through the cracks and drain from the outer wall and the top of the archway. This may be due to the foundation's local deformation and uneven settlement caused by the construction of underground facilities and the surrounding traffic environment, which leads to the pulling and expansion of the foundation wall and the internal rammed soil and the formation of internal cracks. Atmospheric precipitation infiltrates into the interior through the sea plaster and external walls. This leads to more significant wetting and deformation of the compacted loess layer. At the same time, the freeze-thaw cycle in winter intensifies the crack expansion process of the external masonry and internal rammed Earth of the foundation. The deterioration process of water and soil erosion in the foundation of the Xi'an Bell Tower is inevitable and progresses from small to large. This causes visible cracking and water seepage on the exterior walls. Table 1 shown he electrical parameters of the bell tower walls vary widely. Therefore, the GPR method is used to detect the integrity of the masonry, and the erosion degree of the

TABLE 1 Dielectric parameters of common construction materials (Lv et al., 2018b).

	ε_r	ρ S/m	α dB/m	v m/ns
Brick	7	5×10^{-2}	0.4–1	0.118
Loess	3–6	1×10^{-3}~0.1	1–100	0.134
Water	81	1×10^{-4}	2×10^{3}	0.033
Air	1	0	0	0.300

internal rammed Earth layer of the Bell Tower foundation is of great importance for the restoration and protection of this tower. Generally, the GPR method is very useful for restoring and conserving the Xi'an Bell tower.

Experiment

Physical experiment

According to the structure of the Bell Tower pedestal and the characteristics of the disease, we established a two-layer experimental model of masonry-rammed Earth with dielectric properties similar to those of ancient wall bricks. The reflection of GPR signals at the interface between the masonry, wall bricks, and the rammed Earth in contact with the ancient building was studied.

A hypothesis of the physical model of the masonry and the community surface was proposed. Both masonry and rammed Earth are semi-infinite space with continuous homogeneous isotropic perfect dielectric models. The reflection and refraction processes of the geophysical radar waves occur in the two-dimensional plane. The dielectric parameters of the geotechnical model involved in this study are shown in Table 1.

We created a physical experiment model considering the possible existence of the masonry-air interface, masonry-unsaturated soil interface and masonry-water interface in ancient buildings. The physical experiment simulates the reflection characteristics of the interface between masonry structure and air, unsaturated soil, and water, and the physical experiment model and experimental scheme are shown in Figure 3.

The thickness of the masonry is 0.10 m (the thickness of the surface layer of Bell Tower sea plaster is 0.10 m). The height of the specimen box of the bedding layer is 0.15 m. The specimens were air, dry soil, volumetric moisture content (MC) 20%, MC 30%, MC 40%, and pure water.

The instrumentation and parameters were as follows: a SIR3000 series mainframe and high identification antenna with a main frequency of 2 GHz from Geophysical Survey Systems Inc. (GSSI) were used as seen in Figure 3A. The parameters of the equipment settings were an emissivity of 100 KHz and an acquisition mode TIME model. The recording length was 10 ns and the automatic gain point was 5. The 2 GHz antenna was placed on the masonry surface and scanned statically from top to bottom.

The original data (after scanning) for the surface modification and automatic gain available GPR imaging is presented in Figure 2.

As shown in Figure 4, a depth of 0.1 m is the interface between the masonry and each medium. The surface occurs at 0.22 m depth. Figures 4B–F shows that the reflected signal of the GPR wave at the interface gradually increases.

The reflected wave amplitudes from small to large are air, dry soil, unsaturated soil, and water. The reflected wave amplitude images are evaluated quantitatively as well as the amplitude value of the reflection part of the interface in the echo curve. The relative reflection wave amplitudes of different interfaces can be obtained as shown in Table 1 (assuming a maximum reflection amplitude of 1 for the masonry-metal interface).

According to Table 2, the relative echo amplitude of the masonry-air interface is the smallest. The relative wave amplitude of the masonry-unsaturated soil interface gradually increases

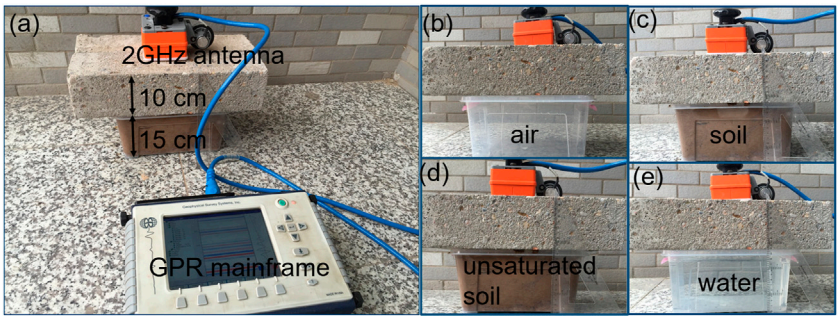

FIGURE 3
Physics experimental equipment and models **(A)** GPR mainframe and physical model; **(B)** concrete-air interface; **(C)** concrete-soil interface; **(D)** concrete-unsaturated soils; and **(E)** concrete-water.

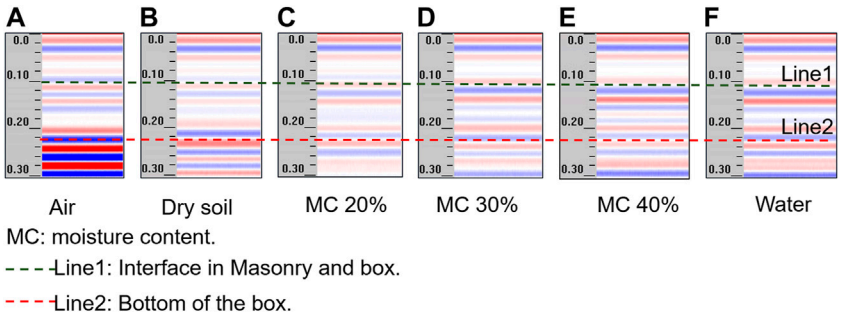

FIGURE 4
Interface reflection result of **(A)** concrete-air; **(B)** concrete-dry soil; **(C)** concrete-MC20% soil; **(D)** concrete-MC30% soil; **(E)** concrete-MC40% soil; and **(F)** concrete-water soil.

TABLE 2 Relative amplitude of the interface reflection (the relative wave amplitude at the masonry-metal interface is 1).

Interface	Air	Dry soil	MC20%	MC30%	MC40%	Water
Amplitude	−0.3531	0.0393	0.2306	0.3348	0.3862	0.492

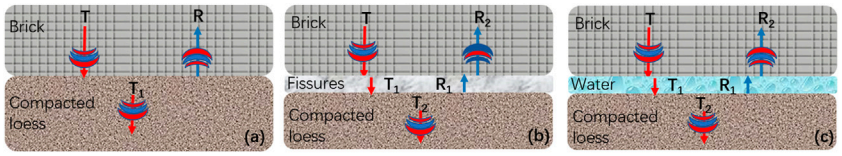

FIGURE 5
Propagation law of electromagnetic waves in **(A)** brick and compacted loess; **(B)** brick and compacted loess with fissures; and **(C)** brick and compacted loess with water fissures.

with an increase of the volumetric water moisture in the specimen. This is because the relative permittivity of the bedding medium gradually increases. Furthermore, the relative permittivity of the surface layer and the relative permittivity of the bedding layer simultaneously change. The variation law of the return amplitude needs more test data, and the physical experimental method is not sufficient to regulate the finer dielectric parameters. Therefore, numerical methods need to be introduced.

Numerical method study of the echo characteristics of the masonry-bedding model

The variation of bedding moisture content in the physical experiments has an effect on the echo amplitude. To reveal the law of change of echo amplitude caused by the change of lithology of the surface layer and the bedding layer, and considering the basic characteristics and properties of the permittivity of the material, an FDTD numerical calculation of the GPR imaging law of the masonry-bedding bilayer media model was conducted. The essential relationship between the material and the echo amplitude and its mechanistic criteria are proposed. A two-layer GPR model was established, and the specific model schematic is shown in Figure 5.

The horizontal distance of this model is 2.0 m and the depth is 0.7 m. The cell size is 0.0025 m by 0.0025. The time depth is 20 ns. The parameters of the first layer are as follows. The permittivity is 0, the electrical conductivity is 0.00 S/m, and the thickness of the first layer is 30 cm. The permittivity of the second layers was 10, 20, 30, 40, and 50. The electrical conductivity is 0.00001 S/m. The thickness of the second layer is 0.4 m. The wavelet frequency is set as 900 MHz, and the excitation source is the Ricker wavelet. In the

10.3389/fmats.2022.952631

TABLE 3 Echo amplitude in the geoelectrical model (the relative wave amplitude at the masonry-metal interface is 1).

Surface cushion	$\varepsilon_1 = 7$	$\varepsilon_1 = 15$	$\varepsilon_1 = 30$	$\varepsilon_1 = 40$
$\varepsilon_2 = 1$	−0.45282	−0.58575	−0.60938	−0.70819
$\varepsilon_2 = 5$	−0.08491	−0.2719	−0.42399	−0.48014
$\varepsilon_2 = 10$	0.09147	−0.10302	−0.27276	−0.33843
$\varepsilon_2 = 15$	0.19338	0	−0.17557	−0.2455
$\varepsilon_2 = 20$	0.26383	0.07406	−0.10377	−0.17597
$\varepsilon_2 = 25$	0.31703	0.13127	−0.04692	−0.12039
$\varepsilon_2 = 30$	0.35939	0.17773	0	−0.07522
$\varepsilon_2 = 35$	0.39436	0.2167	0.04005	−0.03452
$\varepsilon_2 = 40$	0.424	0.25017	0.0748	0
$\varepsilon_2 = 45$	0.44962	0.27942	0.10548	0.03071
$\varepsilon_2 = 50$	0.47212	0.30536	0.13292	0.05822
$\varepsilon_2 = 55$	0.49212	0.32863	0.15772	0.08316
$\varepsilon_2 = 60$	0.5101	0.34969	0.18033	0.10595
$\varepsilon_2 = 65$	0.5256	0.36892	0.20109	0.12693
$\varepsilon_2 = 70$	0.54129	0.3866	0.22026	0.14635
$\varepsilon_2 = 75$	0.55497	0.40293	0.23807	0.16442
$\varepsilon_2 = 80$	0.56764	0.41812	0.25469	0.1813

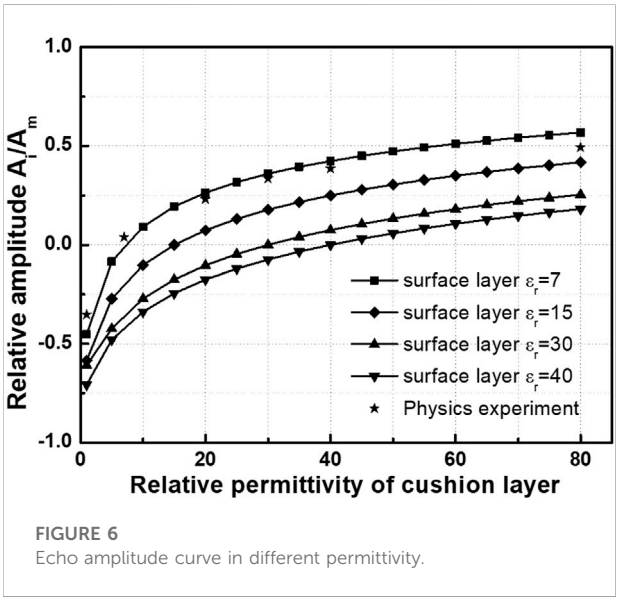

FIGURE 6
Echo amplitude curve in different permittivity.

numerical simulation, there are 180 step calculations and each step calculation contains 3,391 times.

Shown in Table 3. The basic law of echo amplitude is as follows: the surface medium remains unchanged, and when the relative permittivity of the bedding medium increases, the corresponding relative echo amplitude of GPR is also bound to increase. At the same time, when the relative permittivity of the surface layer and the bedding layer are equal, the echo amplitude is 0, which indicates that the electromagnetic wave completely penetrates the interface. According to the wave amplitude characteristics of the two-layer geoelectric model, the basic law can be derived as shown in Figure 6.

In Figure 6, Ai is the GPR echo amplitude, and Am is the GPR echo amplitude at the metal interface. It can be intuitively determined that the smaller the relative permittivity of the surface layer, the larger the relative echo amplitude, which indicates that the imaging characteristics of the bedding defects are more obvious. And comparing the physical experimental data, the basic law and numerical results of the interface reflection test data of physical experiments are the same. Both indicate that the echo amplitude increases as the relative permittivity of the bedding increases. Overall, the results of numerical calculation have high accuracy and a practical application value.

Empirical model of the return amplitude of the double-layer medium

From the findings of physical and numerical experiments, it is clear that the echo amplitude of the double-layered medium is related to the relative permittivity values of both the surface layer and the mat. The echo amplitude of the double-layer medium is related to the relative permittivity values of the surface layer and the bedding layer of the medium. The larger the difference between the relative permittivity of the two sides of the interface, the larger the echo amplitude.

To further directly apply the experimental and numerical results to the field test, this study establishes the mathematical relationship between the difference and the ratio of the relative permittivity and the return amplitude of the double-layer medium and its basic law. An analytical model that is more applicable to the rapid determination of the water moisture of defects in the formation in the field was established.

Figure 7A shows the echo amplitude law of the relative permittivity difference of the media on both sides of the interface. Individual data escapes and the overall law is not obvious. Figure 7B shows the echo amplitude law of the relative permittivity ratio of the media on both sides of the interface. The overall curve is smooth, and there is almost no escape point. This shows that the relative permittivity ratio of the media on both sides of the interface is more accurate than the relative wave amplitude. Therefore, the fitting equation is as follows.

$$A_i/A_m = 0.227 \times \ln(\varepsilon_2/\varepsilon_1) + 0.017 \quad (1)$$

The fill soil of the Bell Tower pedestal bears some of the stress, and the increase in the water moisture of the fill soil must cause a decrease in the mechanical properties of the soil.

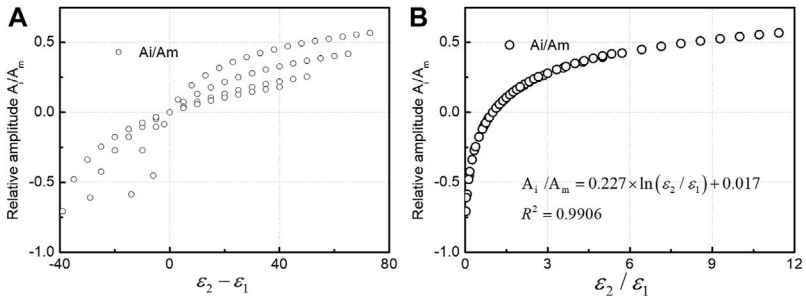

FIGURE 7
Relationship curve of relative amplitude and **(A)** permittivity difference and **(B)** permittivity ratio.

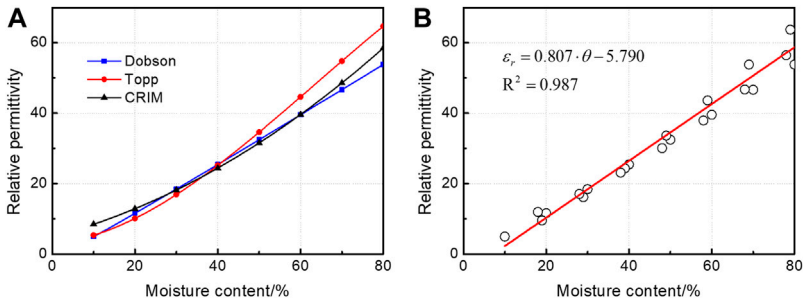

FIGURE 8
(A) Typical empirical relationships curve of permittivity and moisture content and **(B)** relationships curve of permittivity and moisture content of compacted loess.

Water moisture is read more intuitively and quickly from the scanned wave amplitude in this study with the help of Topp's formula (Topp et al., 1980), Dobson's (Dobson et al., 1985) formula, and the Complex Reflective Index Model (CRIM) (Fernandes et al., 2017; Madhousehoush et al., 2021). The laws of water moisture and relative permittivity of soil derived from these commonly used models are compared, and the simple model of water moisture and soil relative permittivity is summarized. These equations are shown in Figure 8A.

Topp's formula

$$\varepsilon_r = 3.03 + 9.3 \times \theta_v + 146.0 \times \theta_v^2 - 76.6 \times \theta_v^3 \quad (2)$$

Dobson's formula

$$\varepsilon_{soil}^{\alpha} = 1 + \frac{\rho_b}{\rho_{ss}}\left(1 - \varepsilon_{ss}^{\alpha}\right) + m_v^{\beta}\left(\varepsilon_{fw}^{\alpha} - 1\right) \quad (3)$$

CRIM formula

$$\sqrt{\varepsilon} = (1 - \phi) \cdot \sqrt{\varepsilon_s} + S_w \cdot \phi \cdot \sqrt{\varepsilon_w} + (1 - S_w) \cdot \phi \cdot \sqrt{\varepsilon_a} \quad (4)$$

In Formula 2, ε_r is the permittivity and θ_v is the volume of moisture content.

In Formula 3, ε_{soil} refers to the soil permittivity. ρ_b and ρ_{ss} refer to the density of dry soil and soil skeleton, respectively. ε_{ss} refers to the solid permittivity. m_v refers to solid quality. ε_{fw} refers to the fluid water permittivity. The empirical coefficient α is 0.65 and β = 1.0 ~ 1.17 (from sandy soil to clay).

In Formula 4, the subscript of *s*, *w*, and *a* represent the soil, water, and air, respectively. φ represents the moisture content, and S_w represents the moisture saturation.

In Figure 8B the relative permittivity of the masonry in the surface layer of the Bell Tower is 7, as measured by calibration, and combined with Eq. 2 and substituted in Eq. 1. The empirical model on water moisture and echo amplitude can be obtained as follows.

$$A_i/A_m = 0.227 \times \ln\frac{0.807 \cdot \theta - 5.790}{7} + 0.017 \quad (5)$$

With Model 5, one can quickly calculate the volumetric water moisture of the soil layer from the relative wave amplitudes in the measured GPR images to observe the water filling of cracks and the dissolution in the loess bedding of the Bell Tower foundation.

TABLE 4 GPR parameter settings.

Parameter	Value
Frequency	400 MHz
Transmit rate	50 kHz
Samp/scan	512
Scans/s	64
Scans/m	20
Ranges	46 ns
Depth	2.0 m
Permittivity	8.0

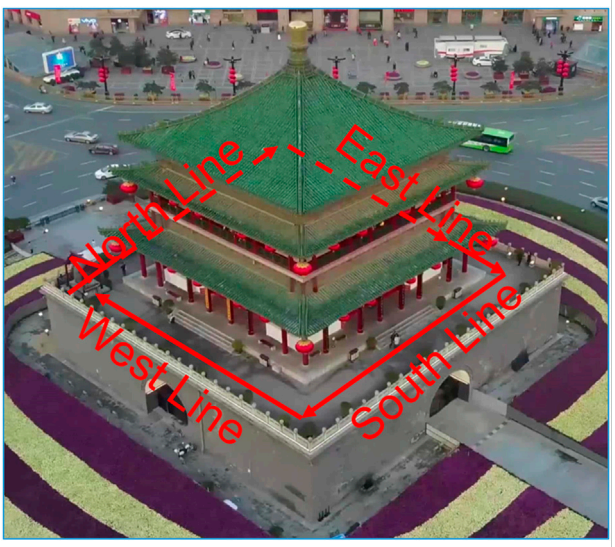

FIGURE 9
Bell Tower abutment survey line layout.

GPR imaging and dielectric property analysis of the Xi'an Bell Tower foundation

Differences in the electromagnetic properties of geotechnical soils are key factors for accurate detection. The water content of the rammed Earth layer at the foundation of the Xi'an Bell Tower tends to be saturated by precipitation. There is a significant difference between the relative permittivity and brick of the rammed soil with saturated water content. Therefore, the conditions for GPR detection are available. In this study, the four sea plasterers of the Xi'an Bell Tower pedestal are scanned by GPR, which can identify and judge the damage of rammed Earth debonding, cracks, and dissolution joints under the masonry structure of the pedestal, and provide accurate information on the location and depth for later repair and maintenance.

GPR field inspection of the Xi'an Bell Tower pedestal

In this study, GSSI's SIR3000 series GPR was used to scan and detect the four sea mantle surfaces of the Bell tower pedestal, and the model and main parameters of the GPR equipment are Shown in Table 4.

The location of the measurement lines is shown in Figure 9, and there are four measurement lines in the southeast and northwest that all have a length of 30 m and a probing depth of 2 m. The measured data were used to analyze the defects in the foundation of the Bell Tower and to investigate the water seepage areas and seepage points inside the foundation of the Bell Tower. The preliminary scanning profile of each mantle surface is shown in Figure 10 by detecting the sea plaster position of the Bell tower foundation.

Figures 10A–D shows the GPR scan profiles of the east, south, west, and north survey lines of the base mantle of Zhong Lou Terrace. Intuitively, there are 16 major anomalous sites among which the anomalous reflections in Figure 10A are: E1~E5; the anomalous reflections in Figure 10B are: S1~S5; the anomalous reflections in Figure 10C are: W1~W3; and the anomalous reflections in Figure 10D are: N1~N3. These significant anomalous reflections can be divided into two categories. The first category as E1, E2, E3, E4, E5, S1, S2, S3, S4, S5, W1, W2, and W3 are hyperbolic winding waves. The reflected waves are discontinuous in the same phase axis and multiple reflections are obvious, which can be inferred to the cavity or the top of the fracture, and the highest point of the hyperbolic curve is the location of the problem. Among them, the hyperbolic curves of E3, E4, S4, W1, W2, and W3 reflect fast attenuation and low frequency and amplitude. The characteristics of fast decay, low frequency, and strong amplitude are reflected in the hyperbolic curves of E3, E4, S4, W1, W2, and W3, and there are a large number of multiple oscillations. The second category as N1, N2, and N3 regions, with intermittent isotropic axes and strong reflections in the region, is inferred to as the area of deglacial anomalies. Among them, the signals at N1 and N2 are disordered and incomplete around the radiated waves with irregular imaging shapes and many prismatic points, which indicates the existence of miscellaneous fillings with high water moisture between the masonry and rammed Earth at this place.

Quantitative analysis of the water moisture of the rammed soil inside the foundation

For data on the four sides of the sea plaster of the Bell Tower foundation, the echo wave amplitude was extracted and substituted into empirical Eq. 5, and the defects and dielectric properties could be inferred as shown in Table 5.

The summary table obtained from the statistics of 16 defects present in the scanned map of the Bell Tower abutment is shown in Table 5. After extracting the wave amplitude values at the top of the

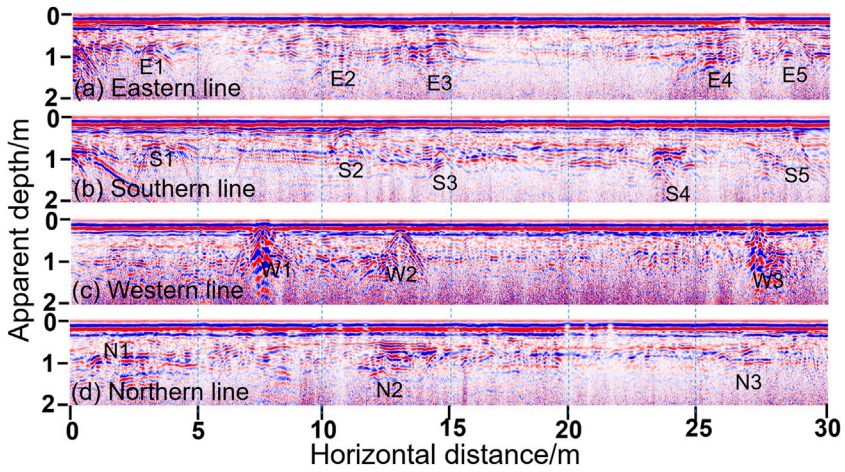

FIGURE 10
(A–D) Scanning profiles of the east, south, west, and north lines of the sea mantle of the Bell Tower.

TABLE 5 Summary of defects and quantification of water moisture of the foundation.

	No.	Horizontal position/m	Relative wave amplitude	Water moisture %
Eastern line	E1	3.0	0.30	38
	E2	10.5	0.05	17
	E3	14.5	0.30	37
	E4	26.0	0.29	36
	E5	29.0	0.02	16
Southern line	S1	3.0	0.24	30
	S2	11.0	0.22	28
	S3	14.5	0.18	25
	S4	24.0	0.29	36
	S5	29.0	0.02	16
Western line	W1	7.5	0.33	42
	W2	13	0.26	33
	W3	27.5	0.32	40
Northern line	N1	2.5	0.28	35
	N2	12.5	0.29	36
	N3	27	0.22	28

anomalous reflection curve and performing the normalization calculation, the quantitative water moisture of the defective parts can be obtained by substituting them into the empirical Model 5. According to the calculated water moisture values of each defect site, it is obvious that the highest volumetric water moisture of more than 40% is found in regions W1 and W3, which indicates that the cracks or cavities have produced larger water seepage channels and water erosion phenomena, and since it is almost impossible for the actual existing cavity defects to be regular in shape, the actual defects are different from the standard hyperbolic features; at E1, E3, E4, N1, N2 and W2, the volumetric water moisture is in the range of 35%–38%, which indicates that the defects also have a greater potential risk, while the volumetric water moisture of the E2 and E5 areas is 16%, which is relatively less risky.

As the Bell Tower was a national key for protection as a culturally famous building, this study only focused on the external wall surface with serious water seepage area photographic evidence, and the most serious internal defects of the western side of the sea plaster position and the external wall water seepage parts coincide.

Conclusion

Through a series of physical experiments and numerical simulation analysis, we obtained the propagation law and characteristics of electromagnetic waves in the double-layer medium and summarized the general empirical formula. The empirical formula was applied to the detection of the Xi'an Bell Tower. A series of structural defects were successfully detected and the main conclusions are drawn as follows.

(1) According to the numerical calculation results of the two-layer geoelectric model, the mathematical and theoretical relationship between the relative permittivity of the mat and the echo amplitude was obtained. We reveal that the laws of the surface layer medium remain unchanged, but the permittivity of the bedding layer medium increases.
(2) The empirical relationship between the permittivity ratio and the echo amplitude has high practicality and accuracy in calculating the water moisture of defects and has a very high application value for the safety evaluation of ancient buildings.
(3) The empirical formula can be considered to have certain practical significance and scientific research value for problem prevention and active monitoring of this type of building. In the next research work, we hope to continuously improve and enrich the accuracy of the empirical formula and perform a practice of validation.

Data availability statement

The raw data supporting the conclusion of this article will be made available by the authors without undue reservation.

Author contributions

GL was in charge of the physical experiments; NL was in charge of the numerical simulations; LB was in charge of collecting field data; and YZ was in charge of the post-processing data and analysis.

Funding

This work was supported by the Shaanxi Key Laboratory of Geotechnical and Underground Space Engineering (Grant no. JT201901), Shaanxi Provincial Urban and Rural Construction Science and Technology Research and Development Program Project (2020-K41), National Natural Science Foundation of China (51806173), Natural Science Foundation of Shaanxi Province (Grant nos. 2021SF-500, 2019M663648, and 2020JM-538), and Open Fund of State Key Laboratory of Road Engineering Safety and Health in Cold and High-altitude Regions (Grant no. YGY2020KYPT-03).

Conflict of interest

The authors declare that the research was conducted in the absence of any commercial or financial relationships that could be construed as a potential conflict of interest.

Publisher's note

All claims expressed in this article are solely those of the authors and do not necessarily represent those of their affiliated organizations, or those of the publisher, the editors and the reviewers. Any product that may be evaluated in this article or claim that may be made by its manufacturer is not guaranteed or endorsed by the publisher.

References

Adachi, S., Yamaguchi, S., Ozeki, T., and Kose, K. (2020). Application of a magnetic resonance imaging method for nondestructive, three-dimensional, high-resolution measurement of the water content of wet snow samples. *Front. Earth Sci. (Lausanne).* 8, 179. doi:10.3389/feart.2020.00179

Adamopoulos, E., and Rinaudo, F. (2021). Close-range sensing and data fusion for built heritage inspection and monitoring—a review. *Remote Sens.* 13 (19), 3936. doi:10.3390/rs13193936

Agliata, R., Bogaard, T. A., Greco, R., Mollo, L., Slob, E. C., and Steele-Dunne, S. C. (2018). Non-invasive estimation of moisture content in tuff bricks by GPR. *Constr. Build. Mater.* 160, 698–706. doi:10.1016/j.conbuildmat.2017.11.103

Bai, B., Yang, G. C., Li, T., and Yang, G. S. (2019). A thermodynamic constitutive model with temperature effect based on particle rearrangement for geomaterials. *Mech. Mater.* 139, 103180. doi:10.1016/j.mechmat.2019.103180

Bai, B., Fei, L., Rao, D., and Xu, T. (2017). The effect of temperature on the seepage transport of suspended particles in a porous medium. *Hydrol. Process.* 31 (2), 382–393. doi:10.1002/hyp.11034

Bai, B., Nie, Q., Zhang, Y., Wang, X., and Hu, W. (2021). Cotransport of heavy metals and SiO2 particles at different temperatures by seepage. *J. Hydrology* 597, 125771. doi:10.1016/j.jhydrol.2020.125771

Bai, B., Wang, Y., Rao, D., and Fan, B. (2022). The effective thermal conductivity of unsaturated porous media is deduced by pore-scale SPH simulation. *Front. Earth Sci.* doi:10.3389/feart.2022.943853

Bai, B., Xu, T., Nie, Q., and Li, P. (2020). Temperature-driven migration of heavy metal Pb2+ along with moisture movement in unsaturated soils. *Int. J. Heat Mass Transf.* 153, 1–12. doi:10.1016/j.ijheatmasstransfer.2020.119573

Bai, B., Zhou, R., Cai, G., Hu, W., and Yang, G. (2021). Coupled thermo-hydro-mechanical mechanism in view of the soil particle rearrangement of granular thermodynamics. *Comput. Geotechnics* 137 (8), 104272. doi:10.1016/j.compgeo.2021.104272

Cappuccio, F., Toy, V. G., Mills, S., and Adam, L., (2020). Three-dimensional separation and characterization of fractures in X-ray computed tomographic images of rocks. *Front. Earth Sci.*, 12, 540. doi:10.3389/feart.2020.529263

Cardinali, V., Castellini, M., Cristofaro, M. T., Lacanna, G., Coli, M., De Stefano, M., et al. (2021). Integrated techniques for the structural assessment of cultural heritage masonry buildings: Application to Palazzo Cocchi-Serristori in Florence. *J. Cult. Herit. Manag. Sustain. Dev.* doi:10.1108/JCHMSD-02-2021-0024

Corradi, M., Di Schino, A., Borri, A., and Rufini, R. (2018). A review of the use of stainless steel for masonry repair and reinforcement. *Constr. Build. Mater.* 181, 335–346. doi:10.1016/j.conbuildmat.2018.06.034

Dao, D. V., Adeli, H., Ly, H. B., Le, L. M., Le, V. M., Le, T. T., et al. (2020). A sensitivity and robustness analysis of GPR and ANN for high-performance concrete compressive strength prediction using a Monte Carlo simulation. *Sustainability* 12 (3), 830. doi:10.3390/su12030830

Dobson, M. C., Ulaby, F. T., Hallikainen, M. T., and El-Rayes, M. A. (1985). Microwave dielectric behavior of wet soil-Part II: Dielectric mixing models. *IEEE Trans. Geosci. Remote Sens.* 23 (1), 35–46. doi:10.1109/tgrs.1985.289498

Elyamani, A., Caselles Magallón, J. O., Roca Fabregat, P., and Clapes, J., (2018). Integrated dynamic and thermography investigation of Mallorca Cathedral. *Mediterr. Archaeol. Archaeom.* 18 (1), 221–236. doi:10.5281/zenodo.1165360

Elyamani, A., Roca Fabregat, P., Caselles Magallón, J. O., and Clapes, J., (2019). Evaluation of Mallorca Cathedral seismic behavior using different analysis techniques. *Mediterr. Archaeol. Archaeom.* 19 (1), 41–60. doi:10.5281/zenodo.2585970

Elyamani, A., Roca, P., Caselles, O., and Clapes, J. (2017). Seismic safety assessment of historical structures using updated numerical models: The case of Mallorca cathedral in Spain. *Eng. Fail. Anal.* 74, 54–79. doi:10.1016/j.engfailanal.2016.12.017

Fediuk, A., Wilken, D., Wunderlich, T., and Rabbel, W. (2020). Physical parameters and contrasts of wooden objects in lacustrine environment: Ground penetrating radar and geoelectrics. *Geosciences* 10 (4), 146. doi:10.3390/geosciences10040146

Fernandes, F. M., Fernandes, A., and Pais, J. (2017). Assessment of the density and moisture content of asphalt mixtures of road pavements. *Constr. Build. Mater.* 154, 1216–1225. doi:10.1016/j.conbuildmat.2017.06.119

Hou, Y., Hu, W., Wang, X., Hou, T., and Sun, C. (2021). Damage identification of ancient timber structure based on autocorrelation function. *Adv. Civ. Eng.*, 2021, 2021–2112. doi:10.1155/2021/6683666

Kang, Y., Fan, J., Jiang, D., and Li, Z. (2021). Influence of geological and environmental factors on the reconsolidation behavior of fine granular salt. *Nat. Resour. Res.* 30 (1), 805–826. doi:10.1007/s11053-020-09732-1

Khan, M. Y., Shafique, M., Turab, S. A., and Ahmed, N., (2021). Characterization of an unstable slope using geophysical, UAV, and geological techniques: Karakoram himalaya, northern Pakistan. *Front. Earth Sci.*, 9, 705. doi:10.3389/feart.2021.668011

Lai, W. W. L., Derobert, X., and Annan, P. (2018). A review of ground penetrating radar application in civil engineering: A 30-year journey from locating and testing to imaging and diagnosis[J]. *NDT E Int.* 96, 58–78.

Lieblappen, R., Fegyveresi, J. M., Courville, Z., and Albert, D. G. (2020). Using ultrasonic waves to determine the microstructure of snow. *Front. Earth Sci. (Lausanne).* 8, 34. doi:10.3389/feart.2020.00034

Liu, N., Li, N., bang, X. C., Li, G., Song, Z., and Yang, M. (2020). Mechanism of secondary lining cracking and its simulation for the dugongling tunnel. *Rock Mech. Rock Eng.* 53 (9), 4539–4558. doi:10.1007/s00603-020-02183-3

Liu, N., Liang, C., and Wang, Y. (2020). Analytical assessment of internal stress in cemented paste backfill. *Adv. Mater. Sci. Eng.* 2020, 1–15. doi:10.1155/2020/6666548

Lombardi, F., Lualdi, M., and Garavaglia, E. (2021). Masonry texture reconstruction for building seismic assessment: Practical evaluation and potentials of Ground Penetrating Radar methodology. *Constr. Build. Mater.* 299, 124189. doi:10.1016/j.conbuildmat.2021.124189

Lu, X., Guan, H., Sun, H., Li, Y., Zhe, Z., Yifan, F., et al. (2021). A preliminary analysis and discussion of the condominium building collapse in surfside, Florida, US, June 24, 2021. *Front. Struct. Civ. Eng.*, 15, 1–14. doi:10.1007/s11709-021-0766-0

Luo, D., Wang, S., Du, X., Zhao, P., Lu, T., Yang, H., et al. (2021). Health detection techniques for historic structures. *Mater. Test.* 63 (9), 855–864. doi:10.1515/mt-2021-0013

Lv, G., Li, N., Yang, J., Yao, X., Hu, D., and Pang, R. (2018). Inversion model of GPR imaging characteristics of point objects and fracture detection of heritage building. *J. Sensors* 2018, 1–10. doi:10.1155/2018/3095427

Lv, G., Yang, J., Li, N., Hu, D., Zhang, Y., and Zhao, F. (2018). Dielectric characteristics of unsaturated loess and the safety detection of the road subgrade based on GPR. *J. Sensors* 2018, 1–8. doi:10.1155/2018/5185460

Ma, G., and Wang, L. (2018). A critical review of preparation design and workability measurement of concrete material for largescale 3D printing. *Front. Struct. Civ. Eng.* 12 (3), 382–400. doi:10.1007/s11709-017-0430-x

Madhousehoush, H., Giannopoulos, A., and Giannakis, I. (2021). "A revised Complex refractive Index model for inferring the permittivity of heterogeneous concrete models," in EGU General Assembly Conference Abstracts. 1-15.

Mishra, M. (2021). Machine learning techniques for structural health monitoring of heritage buildings: A state-of-the-art review and case studies. *J. Cult. Herit.* 47, 227–245. doi:10.1016/j.culher.2020.09.005

Qiu, J., Qin, Y., Feng, Z., Wang, L., and Wang, K. (2020). Safety risks and protection measures for city wall during construction and operation of xi'an metro. *J. Perform. Constr. Facil.* 34 (2), 04020003. doi:10.1061/(asce)cf.1943-5509.0001374

Solla, M., Gonçalves, L., Gonçalves, G., Francisco, C., Puente, I., Providencia, P., et al. (2020). A building information modeling approach to integrate geomatic data for the documentation and preservation of cultural heritage. *Remote Sens.* 12 (24), 4028. doi:10.3390/rs12244028

Stepinac, M., Kisicek, T., Renić, T., Hafner, I., and Bedon, C. (2020). Methods for the assessment of critical properties in existing masonry structures under seismic loads—the ARES project. *Appl. Sci.* 10 (5), 1576. doi:10.3390/app10051576

Topp, G. C., Davis, J. L., and Annan, A. P. (1980). Electromagnetic determination of soil water content: Measurements in coaxial transmission lines. *Water Resour. Res.* 16 (3), 574–582. doi:10.1029/wr016i003p00574

Wang, H., Zhou, B., and Zhang, X. (2017). Research on the remote maintenance system Architecture for the rapid development of smart substation in China. *IEEE Trans. Power Deliv.* 33 (4), 1845–1852. doi:10.1109/tpwrd.2017.2757939

Wang, J., Zhang, Q., Song, Z., and Zhang, Y. (2020). Creep properties and damage constitutive model of salt rock under uniaxial compression. *Int. J. Damage Mech.* 29 (6), 902–922. doi:10.1177/1056789519891768

Wu, X., Senalik, C. A., Wacker, J. P., Wang, X., and Li, G. (2020). Ground-penetrating radar investigation of salvaged timber girders from bridges along route 66 in California. *Wood Fiber Sci.* 52 (1), 73–86. doi:10.22382/wfs-2020-007

Xie, Q., Xu, D., Zhang, Y., Yu, Y., and Hao, W. (2020). Shaking table testing and numerical simulation of the seismic response of a typical China ancient masonry tower. *Bull. Earthq. Eng.* 18 (1), 331–355. doi:10.1007/s10518-019-00731-z

Xue, C. Q. L. (2010). *World architecture in China*. Hong Kong: Joint Publishing.

Zhu, C., Shi, D., Liao, S., He, P., and Jia, R. (2020). Effects of Synechococcus sp. PCC 7942 harboring vp19, vp28, and vp (19 + 28) on the survival and immune response of Litopenaeus vannamei infected WSSV. *Fish. Shellfish Immunol.* 99, 1–8. doi:10.1016/j.fsi.2020.01.028

Ziegler, M. J., Perez, V. J., Pirlo, J., Narducci, R. E., Moran, S. M., Selba, M. C., et al. (2020). Applications of 3D paleontological data at the Florida museum of natural history. *Front. Earth Sci. (Lausanne).* 8, 570. doi:10.3389/feart.2020.600696